Journal of Materials Chemistry A

Accepted Manuscript

ROYAL SOCIETY OF CHEMISTRY

www.rsc.org/materialsA

Table of Contents Entry

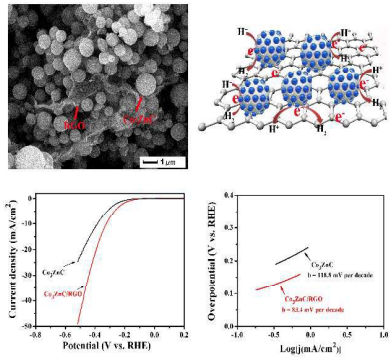

A novel Co_3ZnC/RGO composite with excellent electrocatalytic activity toward HER was prepared through an effective two-step strategy.

Journal Name

RSCPublishing

ARTICLE

Co_3ZnC core-shell nanoparticles assembled microspheres/reduced graphene oxide as an advanced electrocatalyst for hydrogen evolution reaction in acidic solution

Cite this: DOI: 10.1039/xoxxoooooox

Received ooth January 2012,
Accepted ooth January 2012

DOI: 10.1039/xoxxoooooox

www.rsc.org/

Lianbo Ma, Xiaoping Shen,* Jun Zhu, Guoxing Zhu and Zhenyuan Ji

A novel Co_3ZnC/RGO composite with Co_3ZnC microspheres deposited on reduced graphene oxide (RGO) sheets is fabricated through a facile and effective two-step strategy. The Co_3ZnC microspheres with an average diameter of 395 nm have porous structure and are composed of Co_3ZnC core-shell nanoparticles with a size of 24.2 nm. The Co_3ZnC/RGO composite shows a significantly enhanced electrocatalytic activity for hydrogen evolution reaction (HER) with much lower overpotential (108 mV), smaller Tafel slope (83.4 mV per decade) and higher exchange current density (2.1×10^{-2} mA/cm^2) as compared with pure Co_3ZnC catalyst. Besides, the Co_3ZnC/RGO composite exhibits high stability in acidic solution; the HER catalytic activity shows almost no degradation after 1000 cirles. The enhanced performance can be ascribed to the unique porous and core-shell structure of Co_3ZnC as well as the introduction of RGO in Co_3ZnC/RGO composite, which can promote the penetration and migration of the electrolytic ions and improve the electron transfer and transport in electrochemical measurements. This novel approach could be extended to synthesize other carbides/RGO composite nanostructures with excellent electrocatalytic activities for hydrogen generation.

Introduction

The ever increasing global demand for energy and the environmental pollution due to the burning of fossil fuels call for great effort to exploit renewable and clean energy alternatives.[1] Hydrogen, the next generation energy carrier, has attracted much attention due to its high energy storage.[2,3] Splitting of water by either light or electricity is considered to be the most promising way to produce hydrogen.[4] However, due to the existence of a large overpotential for hydrogen evolution reaction (HER), catalysts are usually necessary for increasing the hydrogen production efficiency.[5] Platinum (Pt) group metals are the most efficient catalysts for HER. However, they are noble metals and suffer from a severe shortage in global supply.[6] Therefore, many efforts have been devoted to the search of non-noble metal based HER catalysts with high HER activity in the past decades.

Transition metal chalcogenides,[7-11] phosphides,[12-21] nitrides[22] and carbides[23-26] are the most extensively investigated catalysts for the purpose of replacing Pt group metals because of their high stability, abundance in nature and low cost. However, these catalysts usually suffer from relatively lower electrocatalytic activity toward HER partially due to their intrinsic poor electrical conductivities.[27] Recently, it is acknowledged that the incorporation of these catalysts with carbonaceous materials to construct carbon-based composites is the most efficient way to avoid this limitation.[28] Graphene, which consists of sp^2-bonded aromatic carbon sheets, holds great promise as a conductive additive due to its extraordinary electronic conductivity and huge specific surface area.[29] As a result, the obtained graphene-based composites, such as MoS_2/RGO (RGO = reduced graphene oxide),[30,31] $MoSe_2$/RGO,[32,33] and PdPtS/RGO[34] have been proved to possess greatly enhanced electrocatalytic activity toward HER as compared with their single counterparts.

Among these electrocatalysts, transition metals carbides are the most promising electrocatalysts for HER in acidic solution due to their intrinsic nature.[35,36] However, their synthesis process usually involves harsh experimental conditions and complicated steps, and there is a big difficulty in the combination of transition metal carbides and graphene. For instance, tungsten carbide nanocrystals were synthesized through the solid-state reaction of tungsten precursors with

mesoporous graphitic C_3N_4 as the reactive template in a flow of inert gas at high temperatures of 800-1100 °C.[37] Up to date, almost no reports have focused on transition metal carbides/graphene electrocatalysts. In addition, the electrocatalytic efficiency is also affected by the size, morphology and microstructure of electrocatalysts. The porous and/or core-shell nanostructure favors the penetration and migration of the electrolyte ions, and thus ensures the enough contact between the electrolyte and the catalysts.[38] In this manuscript, a facile and effective two-step strategy was developed to fabricate the composite electrocatalyst of Co_3ZnC/RGO, in which the porous Co_3ZnC hierarchical microspheres assembled by core-shell structured Co_3ZnC nanoparticles are wrapped by RGO sheets. The as-synthesized Co_3ZnC/RGO composites exhibit greatly enhanced electrocatalytic activity toward HER as compared with single pure Co_3ZnC.

Experimental

Chemicals and synthesis

All Chemicals in this work are of analytical purity and used without further purification. Graphite oxide was prepared from natural flake graphite using a modified Hummers method.[39] In a typical synthesis, 0.60 mmol of $Zn(Ac)_2{\cdot}2H_2O$ and 0.40 g of polyvinylpyrrolidone (PVP) were dissolved in 20 mL of deionized water with ultrasonication to form a transparent solution. Then, 0.40 mmol of $K_3[Co(CN)_6]$ dissolved in 20 mL of deionized water was added into the above solution gradually under ultrasonication, and the resulting mixture was further stirred in an ice-water bath for 1 h. Subsequently, a certain amount of graphene oxide (GO) solution (5 mg/mL) was added into the mixture under vigorous stirring at room temperature. After stirring for 6 h, the precipitate was collected through centrifugation, washed with deionized water for several times and dried at 45 °C in a vacuum oven for 24 h. In order to obtain the final products, the powders were pyrolyzed at 600 °C for 2 h in N_2 atmosphere with a heating rate of 3 °C/min. Finally, the system was allowed to cool down to room temperature spontaneously and the products were collected for characterization. The products were designated as Co_3ZnC/RGO-2, Co_3ZnC/RGO-4, Co_3ZnC/RGO-6 and Co_3ZnC/RGO-8 for the introduction of 2, 4, 6 and 8 mL of GO solution, respectively. For comparison, pure Co_3ZnC was prepared in the same way as the Co_3ZnC/RGO composites but without introduction of GO solution in the synthesis process. Bare RGO was also prepared by annealing graphite oxide at 600 °C for 2 h in N_2 atmosphere.

Instrumentation and characterization

The phase structure of the as-synthesized samples were characterized by powder X-ray diffraction (XRD) on a Bruker D-8 Advance diffractometer using Cu *K*α (λ = 1.5406 Å) radiation. The compositions of the products were determined by energy-dispersive X-ray spectrometry (EDS), inductively coupled plasma optical emission spectrometry (ICP-OES, Vista-MPX) and elemental analysis (Perkin-Elmer 240C). EDS was recorded with an energy dispersive spectrometer attached to the scanning electron microscope (JSM-6480). The morphology, size and microstructure of the products were examined by field emission scanning electron microscopy (FESEM, JSM-6480) and transmission electron microscopy (TEM, JEM-2100). Raman scattering was performed on a DXR Raman spectrometer using a 532 nm laser source.

Electrochemical measurements

The catalytic activities of the as-prepared composites toward HER were conducted on a typical three-electrode setup using a CHI 760 D electrochemical analyzer (Chen Hua Instruments, Shanghai, China) at room temperature. Saturated calomel electrode (SCE) and Pt foil were used as the reference and counter electrodes, respectively. Glassy carbon electrode (GCE, 3 mm in diameter) coated with the as-prepared samples (Co_3ZnC/RGO composites, Co_3ZnC or RGO) were used as the working electrodes. Prior to the surface coating, the GCE was polished using 0.05 μm alumina powder, followed by sonication in absolute ethanol, and then allowed to dry at room temperature. For the fabrication of working electrode, catalyst ink was prepared by dispersing 5.0 mg of catalyst into a mixed solvent containing 0.98 mL of absolute ethanol and 20 μL of 5 wt% Nafion solution, and then the mixture was sonicated for about 30 min to form a homogeneous ink. Then 4 μL of the catalyst ink was loaded onto GCE and dried at room temperature naturally. Before the electrochemical measurement, the electrolyte (0.5 M H_2SO_4) was degassed by bubbling nitrogen for about 60 min. Linear sweep voltammetry (LSV) was then conducted at the scan rate of 2 mV s^{-1}. All the potentials reported in our work were calibrated with the reversible hydrogen electrode (RHE). The potential was converted to the RHE electrode according to the equation: E (RHE) = E (SCE) + 0.281 V.

Results and discussion

The formation of Co_3ZnC/RGO composites

In this work, we developed a facile and effective two-step strategy to synthesize Co_3ZnC/RGO composites (Scheme 1). Firstly, $Zn_3[Co(CN)_6]_2$ nanoparticles (Fig. S1, see Supporting Information) were formed through the reaction between Zn^{2+} and $[Co(CN)_6]^{3-}$, and then the $Zn_3[Co(CN)_6]_2$ nanoparticles aggregated together to form $Zn_3[Co(CN)_6]_2$ microspheres due to the presence of PVP.[40] It is acknowledged that GO sheets are highly negatively charged because of the ionization of the carboxylic and phenolic hydroxyl groups on their edges and surface.[41,42] When GO solution was introduced into the reaction system, the positively charged $Zn_3[Co(CN)_6]_2$ microspheres were adsorbed onto GO sheets through the electrostatic interactions. As a result, $Zn_3[Co(CN)_6]_2$/GO composites were formed. When the $Zn_3[Co(CN)_6]_2$/GO composites were pyrolyzed at 600 °C in N_2 atmosphere, the $Zn_3[Co(CN)_6]_2$

microspheres were transformed into porous Co_3ZnC microspheres consisting of Co_3ZnC core-shell nanoparticles. At the same time, GO was converted into RGO *via* the high temperature thermal reduction.[43,44] Therefore, Co_3ZnC/RGO composites with Co_3ZnC microspheres deposited on RGO sheets were obtained.

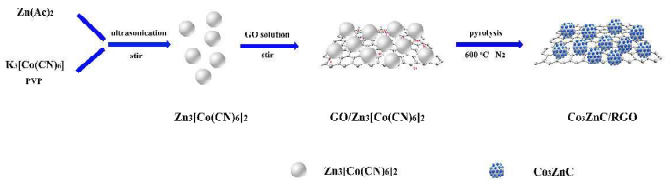

Scheme 1 Illustration of the formation process of Co_3ZnC/RGO composites.

Characterization of Co_3ZnC/RGO composites

XRD patterns of the as-prepared samples are shown in Fig. 1. The original graphite oxide shows a sharp diffraction peak at 2θ = 10.3º, corresponding to the (001) reflection. After the high temperature thermal reduction, the (001) reflection disappeared in the XRD pattern of RGO, while a weak and wide diffraction peak at about 24.6º was detected, which is attributed to the (002) reflection of graphene nanosheets, demonstrating that GO is well reduced in the pyrolysis process.[45] In the XRD patterns of Co_3ZnC and Co_3ZnC/RGO-6, the conspicuous diffraction peaks at 2θ values of 41.9º, 48.8º and 71.5º can be indexed to the (111), (200) and (220) planes of cubic phase Co_3ZnC (JCPDS No. 29-0524), respectively, confirming the formation of Co_3ZnC. The disappearance of the (002) reflection of graphene nanosheets in the XRD pattern of Co_3ZnC/RGO-6 revealed that the stacking of RGO sheets was effectively inhibited by Co_3ZnC microspheres.

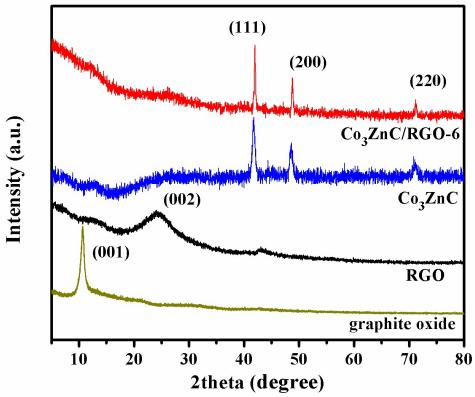

Fig. 1 XRD patterns of graphite oxide, RGO, Co_3ZnC and Co_3ZnC/RGO-6 composite.

The EDS spectrum of the Co_3ZnC/RGO-6 composite is presented in Fig. S2 (see Supporting Information). Carbon, oxygen, cobalt and zinc elements were detected. The atomic ratio of Co to Zn was found to be almost 3:1, which is well consistent with that of Co_3ZnC. The actual contents of Co, Zn and C in the Co_3ZnC/RGO composites were determined by ICP-OES and elemental analysis (see Table S1 in the Supporting Information). It was found that the molar ratios of Co to Zn in the Co_3ZnC/RGO composites are in the range of 2.90-3.30, and the contents of carbon gradually increase from 28.2 to 50.2% with the increasing volume of GO solution used in the synthesis. Moreover, it should be noted that the elemental analysis also revealed the existence of N element in these samples, which may originate from the PVP and CN^-. The presence of N element in Co_3ZnC/RGO products could be beneficial to the improvement of HER activity.[35]

The morphology, size and microstructure of the as-synthesized samples were then characterized by FESEM, TEM and high-resolution TEM (HRTEM). The FESEM images of the precursor, GO/$Zn_3[Co(CN)_6]_2$, are shown in Fig. 2. The precursor is composed of sub-microspheres with an average diameter of 460 nm (Inset of Fig. 2a), and some GO sheets can be clearly identified (as marked with red arrows in Fig. 2a). The surface of the spheres is rough (Fig. 2b), suggesting that the spheres were assembled with smaller particles. The FESEM images of pure $Zn_3[Co(CN)_6]_2$ product synthesized without GO are shown in Fig. S3 (see Supporting Information), from which the microspheres with bigger sizes are observed. This result demonstrates that the presence of GO sheets can reduce the size of the as-synthesized $Zn_3[Co(CN)_6]_2$ particles, which is consistent with a wide range of graphene-based composites reported previously.[34,39,43]

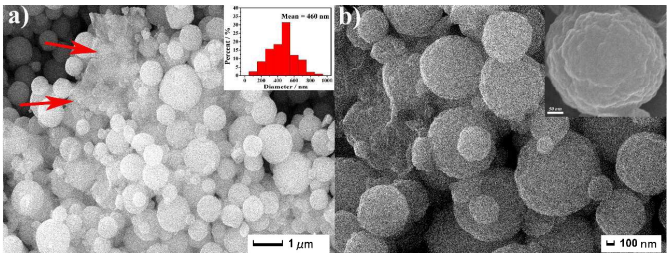

Fig. 2 (a,b) FESEM images of the precursor for Co_3ZnC/RGO-6 composite. The inset of (a) displays the size distribution diagram of the spheres, and the inset of (b) presents a magnified view of the sphere.

Fig. 3 presents the typical FESEM/TEM images of Co_3ZnC/RGO-6 composite. Regular microspheres and silk-like sheets are observed in the FESEM images (Fig. 3a and b), suggesting that the morphology of the GO/$Zn_3[Co(CN)_6]_2$ precursor is well maintained after the annealing treatment. The as-obtained Co_3ZnC microspheres are partly wrapped by RGO sheets, and have an average diameter of about 395 nm (inset of Fig. 3a), which is smaller than the $Zn_3[Co(CN)_6]_2$ microspheres in the precursor, exhibiting that an obvious shrinkage occurs during the pyrolysis process due to the decomposition of $Zn_3[Co(CN)_6]_2$. Moreover, in comparison with the precursor, the Co_3ZnC microspheres show rougher surfaces (Fig. 3b). The elements mapping of the microsphere is presented in Fig. S4a (see Supporting Information), which reveals the presence of the

C, Co, Zn, N and O elements. This is in good agreement with the results of the EDS and element analysis.

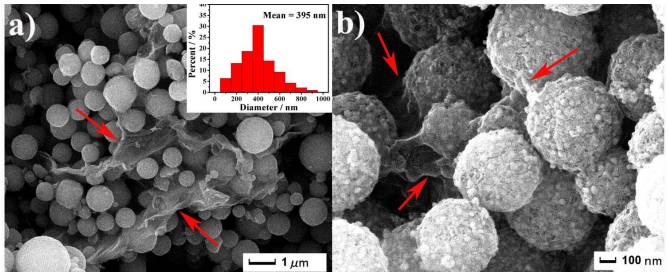

Fig. 3 (a, b) FESEM images of Co_3ZnC/RGO-6 composite. The insets of (a) shows the size distribution diagram of the Co_3ZnC microspheres.

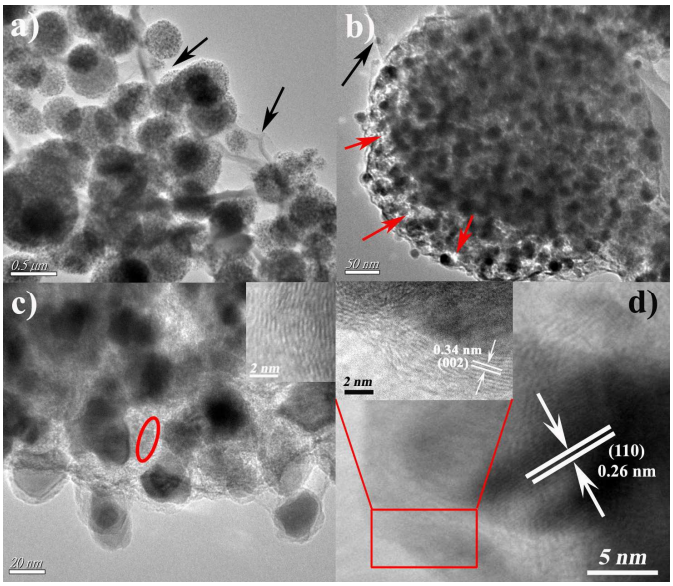

Fig. 4 (a-c) TEM and (d) HRTEM images of Co_3ZnC/RGO-6 composite. The inset of (c) presents the HRTEM image of the domain marked by the red circle, and the inset of (d) shows the HRTRM result of the red rectangle area.

TEM technique was then carried out to further study the microstructure of the microspheres. Fig. 4 shows the TEM images of the Co_3ZnC/RGO-6 composite. Graphene sheets can be clearly observed in them, as marked with black arrows (Fig. 4a and 4b), which is in good agreement with the FESEM observation (Fig. 3). Fig. 4b presents a magnified view of the microsphere, and it reveals that the microsphere is actually composed of amounts of smaller nanoparticles. Nanosized pores with lower contrasts can be observed in the surface of the microspheres, as marked with red arrows. Evidently, the pores should result from the gases released from the decomposition of the precursor during the pyrolysis process. Fig. 4c shows the typical structure of the nanoparticles, it reveals that the nanoparticles possess a core-shell structure. The cores have an average size of 24.2 nm (Fig. S5, see Supporting Information), while that of the shells is about several nanometers in thickness. Moreover, the HRTEM observation (inset of Fig. 4c) indicates the existence of graphitic carbon layers among these Co_3ZnC core-shell nanoparticles, as marked by the red circle. The graphitic carbon network can act as the conductive channels, and thus favors the electron transfer in electrochemical measurements. The HRTEM image (Fig. 4d) of the core-shell structure reveals that the shell of the nanoparticle consists of ordered graphitic layers with a lattice spacing of about 0.34 nm (inset of Fig. 4d), corresponding to the (002) plane of graphite, while the observed lattice spacing of 0.26 nm in the core matches well with the (110) plane of cubic Co_3ZnC, indicating that the core-shell nanoparticles are composed of carbon shells and Co_3ZnC cores. FESEM images of other Co_3ZnC/RGO composites with different RGO contents (Fig. S6, see Supporting Information) display the similar morphology as observed from Co_3ZnC/RGO-6 composite. For comparison, the FESEM and TEM images of pure Co_3ZnC sample are also shown in Fig. S7 (see Supporting Information), the observed Co_3ZnC microspheres show bigger sizes as compared with those in Co_3ZnC/RGO-6 composite. Moreover, the selected area electron diffraction (SAED) patterns (Fig. S4b and S4c, see Supporting Information) of Co_3ZnC/RGO-6 composite and bare Co_3ZnC confirm the polycrystalline nature of the Co_3ZnC particles.

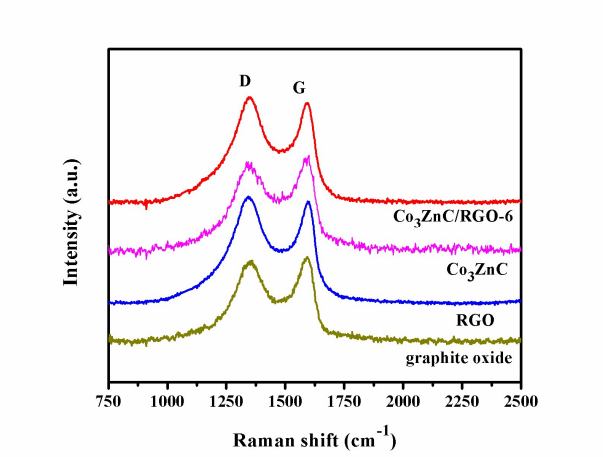

Fig. 5 Raman spectra of graphite oxide, RGO, Co_3ZnC and Co_3ZnC/RGO-6 composite.

Raman spectroscopy is a widely used tool for characterizing the structural properties of carbon-based materials, such as the disorder and defect structures. The typical Raman spectra of the graphite oxide, RGO, Co_3ZnC and Co_3ZnC/RGO-6 composite are shown in Fig. 5. All the spectra show two prominent peaks, which can be ascribed to the well-documented D and G bands.[46] The D band, appears at about 1350 cm^{-1}, is associated with the structure defects and disorders that can break the symmetry and selection rule, while the G band, observed at about 1580 cm^{-1}, is usually assigned to the E_{2g} phonon of sp^2 C atoms corresponding to the stretching vibrations in the basal plane of single-crystal graphene.[47-49] The appearance of the D and G bands in the Raman spectrum of Co_3ZnC confirmed the existence of the graphitic carbon,[50-52] which is well consistent with the TEM observation (Fig. 4e).

The intensity ratio of D to G band, namely the I_D/I_G ratio, is correlative with the average size of the sp^2 domains. The smaller the sp^2 domain is, the higher the I_D/I_G ratio.[53-55] The values of the I_D/I_G ratio for graphite oxide, RGO, Co_3ZnC and Co_3ZnC/RGO-6 composite are *ca.* 1.93, 2.31, 2.04 and 2.42, respectively. In comparison with graphite oxide, the Raman spectrum of RGO shows a higher I_D/I_G ratio, suggesting that GO has been well deoxygenated and reduced under the experimental conditions.[43] Moreover, the I_D/I_G ratio for the Co_3ZnC/RGO-6 composite is further increased as compared with that of RGO. This can be attributed to the Co_3ZnC spheres on RGO sheets, which can stress its surface and induce more defects.[56]

Electrocatalytic activity of Co_3ZnC/RGO composites toward HER

Considering the unique hierarchical architecture and special composition, the as-prepared Co_3ZnC/RGO composites were investigated as the electrocatalysts for HER. The Co_3ZnC/RGO composites, pure Co_3ZnC and bare RGO were respectively deposited onto GCEs with the same loading amount of 0.29 g/cm^2. The HER activities were measured in 0.5 M H_2SO_4 solution using a typical three-electrode setup. Fig. 6a presents the LSV polarization curves of the Co_3ZnC/RGO composites, pure Co_3ZnC and bare RGO electrodes. As a control experiment, the electrochemical performance of commercial Pt/C electrode (20 wt%) was also investigated for comparison. Obviously, the Pt/C electrode shows the lowest overpotential, indicating the highest electrocatalytic activity for HER.[35] The relatively small onset overpotential of Co_3ZnC electrode (193 mV) suggests that Co_3ZnC is a good HER electrocatalyst candidate. The intrinsic properties and unique nanostructures that the Co_3ZnC owns, which can promote the penetration of electrolytic ions into the catalysts and allow more active sites accessible for HER, may be responsible for the great electrocatalytic activity.[57] In comparison with the Co_3ZnC electrode, the Co_3ZnC/RGO electrodes show lower onset overpotentials, indicating that Co_3ZnC/RGO electrodes possess better electrocatalytic activities toward HER.[58-60] Among these Co_3ZnC/RGO electrodes, the Co_3ZnC/RGO-6 electrode exhibits the smallest onset overpotential of 108 mV, and achieves a large current density of 44.6 mA/cm^2 at the overpotential of 0.5 V. Fig. S8 (see Supporting Information) is an optical photograph of the Co_3ZnC/RGO-6 electrode during the LSV scan, showing the production of many hydrogen bubbles on the electrode surface. This phenomenon directly reflects the high electrocatalytic efficiency of the Co_3ZnC/RGO composite catalyst for HER. The greatly enhanced electrocatalytic activities of Co_3ZnC/RGO composites than pure Co_3ZnC toward HER can be attributed to the presence of RGO sheets. On one hand, the excellent electrical properties of RGO could significantly improve the conductivity of the Co_3ZnC/RGO composites, which can boost the electron transport and transfer during HER. This could be the prominent factor responsible for the enhancement of the electrocatalytic activity. On the other hand, the size effect on the electrocatalytic activity cannot be ignored. As shown above, the incorporation of GO sheets in GO/$Zn_3[Co(CN)_6]_2$ composites can reduce the size of the as-formed $Zn_3[Co(CN)_6]_2$ microspheres, thus leading to smaller Co_3ZnC microspheres.[61] The smaller Co_3ZnC microspheres in the hybrid favor the exposure of more active sites for HER.[62,63] These results further prove the advantages of RGO sheets as a direct substrate for the growth of catalyst active components, offering excellent electronic behavior and increasing active sites for HER.

In addition, it is notable that the contents of RGO in Co_3ZnC/RGO composites also have an influence on their electrocatalytic activity for HER. With the increasing RGO content in Co_3ZnC/RGO composites, the electrocatalytic activity increases at first and then decreases. The increment in the electrocatalytic activity toward HER is mainly attributed to the increased electrical conductivity of Co_3ZnC/RGO composites. However, with the further increase of RGO content in the final product, although the electrical conductivity can be unceasingly improved by RGO, the content of catalyst active component (Co_3ZnC) will accordingly reduce. Moreover, the introduction of RGO sheets can also cover the active sites of the catalyst. Thus, the RGO content in Co_3ZnC/RGO composites is crucial to optimize the electrocatalytic activity for HER. For better comparison, the electrocatalytic performances of the Co_3ZnC/RGO-6 catalyst in neutral (phosphate buffered saline (PBS, PH = 7)) and basic (1 M KOH) solutions were also investigated, and the results are shown in Fig. S9 (see Supporting Information). It can be seen that the as-prepared electrocatalysts show high electrocatalytic activity in both neutral and basic solutions, further indicating that the electrocatalyst possesses promising applications in practical hydrogen generation.

Based on the LSV polarization curves of the Co_3ZnC/RGO composites and pure Co_3ZnC electrodes, the corresponding Tafel plots were calculated. As shown in Fig. 6b, the linear regions of the Tafel plots are fitted well to the Tafel equation ($\eta = b \log j + a$, where b is the Tafel slope and j is the current density). The parameters about the HER activity estimated from the Tafel plots are summarized in Table S2 (see Supporting Information). It can be seen that the Co_3ZnC/RGO-6 electrode exhibits the smallest Tafel slope of 83.4 mV per decade, while the largest Tafel slope of 118.8 mV per decade is obtained for the Co_3ZnC electrode. According to the classical two-electron-reaction models, cathodic hydrogen evolution in acidic aqueous media is believed to take place in two steps:[64,65] first, the "discharge step", in which an electron transfers to a proton at the catalyst surface on the cathode, providing an intermediate state of a hydrogen atom bound to an active site (the Volmer reaction: $H^+_{(aq)} + e^- \rightarrow H_{ads}$). The second step is the electrochemical desorption step (the Heyrovsky reaction: $H_{ads} + H^+_{(aq)} + e^- \rightarrow H_{2(g)}$) or the Tafel recombination reaction (Tafel reaction: $H_{ads} + H_{ads} \rightarrow H_{2(g)}$), where H_{ads} represents the H atom absorbed at the active site of the catalyst. The Tafel slope is often utilized as an indication of the dominant mechanism.[26] The rate determining step in the HER process can be assigned

to a Volmer, Heyrovsky, or Tafel reaction by a Tafel slope of 116, 38, or 29 mV per decade. The obtained Tafel slope of Co_3ZnC/RGO-6 composite suggests that the HER on the surface of Co_3ZnC/RGO-6 might follow a Volmer-Heyrovsky mechanism.[38,66] In comparison with Pt/C electrocatalyst (37.2 mV per decade) in this work and most of the reported Pt metal group-related catalysts (Table S3, see Supporting Information),[15,39,67-72] the Co_3ZnC/RGO-6 composite shows slightly lower electrocatalytic activity. However, the electrocatalytic activity of Co_3ZnC/RGO-6 electrocatalyst is comparable to the reported Pd,[71] Pd/C,[72] and PdAu/C[72] electrocatalysts. These results demonstrate that the Co_3ZnC/RGO-6 composite is a promising electrocatalyst for practical HER application.

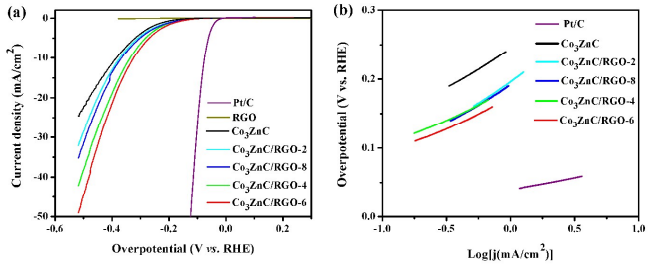

Fig. 6 (a) LSV polarization curves of Co_3ZnC/RGO composites, Co_3ZnC, RGO and Pt/C as the electrocatalysts, and (b) the corresponding Tafel plots of Co_3ZnC/RGO composites, Co_3ZnC and Pt/C electrocatalysts.

In addition, the iR-corrected LSV polarization curves of the Co_3ZnC/RGO composites and the Co_3ZnC microspheres as well as the corresponding Tafel plots are also provided in Fig. S10 (see Supporting Information). It reveals that the Co_3ZnC/RGO catalysts show better electrocatalytic activities than pure Co_3ZnC microspheres, and Co_3ZnC/RGO-6 exhibits the highest electrocatalytic activity. These results are in good agreement with the results obtained from the LSV polarization curves without iR-correction.

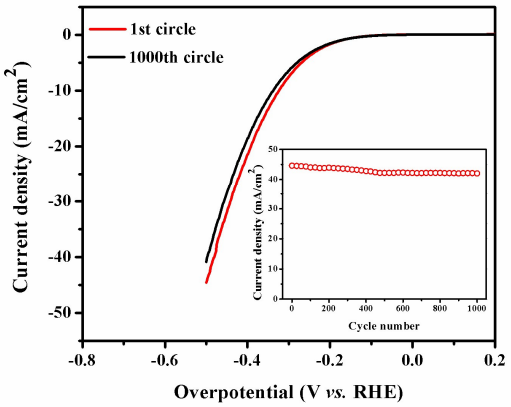

Fig. 7 LSV polarization curves of Co_3ZnC/RGO-6 electrode at the 1st and the 1000th circles between +0.2 and -0.5 V at the scan rate of 20 mV s^{-1}. The inset shows the circle-dependent current density curve for Co_3ZnC/RGO-6 at η = -0.5 V.

The exchange current density (j_0) of the electrode can be used to estimate the electrocatalytic activity of the electrode, a larger exchange current density represents better electrocatalytic activity.[35,73] The j_0 value for the Co_3ZnC/RGO-6 electrocatalyst is *ca.* 2.1×10^{-2} mA/cm^2, which is 2.5 times higher than that of pure Co_3ZnC electrocatalyst (8.7×10^{-3} mA/cm^2). Moreover, we calculated the turnover frequency (TOF) of the electrodes, which is a key parameter to evaluate the activity of an electrocatalyst. The TOFs for the HER in 0.5 M H_2SO_4 solution were calculated by Eric J. Popczun's method at η = -200 mV, and the values for Co_3ZnC/RGO-6 and Co_3ZnC are about 0.0081 and 0.0038 s^{-1}, respectively.[12] These results demonstrate that the Co_3ZnC/RGO electrodes possess better electrocatalytic activity toward HER.

In order to investigate the electrocatalytic stability of the Co_3ZnC/RGO catalysts for HER, the LSV polarization measurements of Co_3ZnC/RGO-6 electrode were repeated for 500 times in 0.5 M H_2SO_4 solution, and the results are shown in Fig. 7. It can be seen that the current density of the Co_3ZnC/RGO-6 electrode at η = 0.5 V shows a slight decrease from 44.6 to 42.2 mA/cm^2 within the first 500 circles, and then it remains stable in the residual circles, suggesting that the as-prepared Co_3ZnC/RGO composites exhibit extraordinary electrochemical stability in acidic solutions. In contrast, pure Co_3ZnC exhibits an obvious deterioration of current density within 500 circles (Fig. S11, see Supporting Information). However, after 500 circles, the Co_3ZnC catalyst was then scraped from the GCE for SEM/TEM observation, as shown in Fig. S12 (see Supporting Information), the unique microspheric structure is well maintained after the long circles. Therefore, the difference in electrochemical stability can be attributed to the formation of hybrid nanostructures and to the chemical and electronic coupling interactions between Co_3ZnC microspheres and RGO sheets.[74] These results further confirm that the Co_3ZnC/RGO catalysts hold great promise for HER application.

Conclusions

In summary, a novel Co_3ZnC/RGO composite with Co_3ZnC microspheres deposited on RGO sheets was synthesized through a facile and effective two-step strategy. The Co_3ZnC microspheres were composed of Co_3ZnC nanoparticles with interconnected carbon networks. It was revealed that the contents of RGO in Co_3ZnC/RGO composites have a great influence on their electrocatalytic activities toward HER. The Co_3ZnC/RGO composite shows a significantly enhanced electrocatalytic activity with a lower overpotential (108 mV), smaller Tafel slope (83.4 mV per decade) and larger exchange current density (2.1×10^{-2} mA/cm^2) as compared with that of pure Co_3ZnC catalyst. Moreover, extremely high electrochemical stability of Co_3ZnC/RGO composite toward HER was obtained. These results can be attributed to the unique porous and hybrid nanostructures that the Co_3ZnC microspheres own, as well as the presence of RGO in Co_3ZnC/RGO composite. It is expected that this composite could supply a new type of electrocatalyst for electrochemical

hydrogen generation. Moreover, this synthetic strategy provides a facile route for constructing other composites with unique nanostructures and particular compositions.

Acknowledgements

The authors are grateful for financial support from National Nature Science Foundation of China (No. 51072071, 51272094, 51102117) and Specialized Research Fund for the Doctoral Program of Higher Education of China (No. 20123227110018).

Notes and references

School of Chemistry and Chemical Engineering, Jiangsu University, Zhenjiang 212013, P. R. China, Fax: (+86)511-88791800; Tel: (+86)511-88791800; E-mail: xiaopingshen@163.com

1 X. L. Zheng, J. B. Xu, K. Y. Yan, H. Wang, Z. L. Wang and S. H. Yang, *Chem. Mater.,* 2014, **26**, 2334.
2 T. R. Cook, D. K. Dogutan, S. Y. Reece, Y. Surendranath, T. S. Teet and D. G. Nocera, *Chem. Rev.,* 2010, **110**, 6474.
3 A. I. Hochbaum and P. Yang, *Chem. Rev.,* 2010, **110**, 527.
4 M. G. Walter, E. L. Warren, J. R. McKone, S. W. Boettcher, Q. X. Mi, E. A. Santori and N. S. Lewis, *Chem. Rev.,* 2010, **110**, 6446.
5 Z. Y. Lu, H. C. Zhang, W. Zhu, X. Y. Yu, Y. Kuang, Z. Chang, X. D. Lei and X. M. Sun, *Chem. Commun.,* 2013, **49**, 7516.
6 E. Antolini, *Energy Environ. Sci.,* 2009, **2**, 915.
7 B. Hinnemann, P. G. Moses, J. Bonde, K. P. Jorgensen, J. H. Nielsen, S. Horch, I. Chorkendorff and J. K. Norskov, *J. Am. Chem. Soc.,* 2005, **127**, 5308.
8 J. F. Xie, H. Zhang, S. Li, R. X. Wang, X. Sun, M. Zhou, J. F. Zhou, X. W. Lou and Y. Xie, *Adv. Mater.,* 2013, **25**, 5807.
9 H. I. Karunadasa, E. Montalvo, Y. J. Sun, M. Majda, J. R. Long and C. J. Chang, *Science,* 2012, **335**, 698.
10 D. S. Kong, H. T. Wang, J. J. Cha, M. Pasta, K. J. Koski, J. Yao and Y. Cui, *Nano Lett.,* 2013, **13**, 1341.
11 H. T. Wang, D. S. Kong, P. Johanes, J. J. Cha, G. Y. Zheng, K. Yan, N. A. Liu and Y. Cui, *Nano Lett.,* 2013, **13**, 3426.
12 E. J. Popczun, J. R. McKone, C. G. Read, A. J. Biacchi, A. M. Wiltrout, N. S. Lewis and R. E. Schaak, *J. Am. Chem. Soc.,* 2013, **135**, 9267.
13 H. F. Du, Q. Liu, N. Y. Cheng, A. M. Asiri, X. P. Sun and C. M. Li, *J. Mater. Chem. A,* 2014, **2**, 14812.
14 J. Q. Tian, Q. Liu, A. M. Asiri and X. P. Sun, *J. Am. Chem. Soc.*, 2014, **136**, 7587.
15 J. Q. Tian, Q. Liu, N. Y. Cheng, A. M. Asiri and X. P. Sun, *Angew. Chem. Int. Ed.*, 2014, **53**, 9577.
16 P. Jiang, Q. Liu, Y. H. Liang, J. Q. Tian, A. M. Asiri and X. P. Sun, *Angew. Chem. Int. Ed.*, 2014，**53**, 12855.
17 Z. C. Xing, Q. Liu, A. M. Asiri and X. P. Sun, *Adv. Mater.*, 2014, **26**, 5702.
18 Z. C. Xing, Q. Liu, A. M. Asiri and X. P. Sun, *ACS Catal.*, 2015, **5**, 145.
19 Z. H. Pu, Q. Liu, P. Jiang, A. M. Asiri, A. Y. Obaid and X. P. Sun, *Chem. Mater.*, 2014, **26**, 4326.
20 Z. H. Pu, Q. Liu, C. Tang, A. M. Asiri and X. P. Sun, *Nanoscale*, 2014, **6**, 11031.
21 P. Jiang, Q. Liu and X. P. Sun, *Nanoscale*, 2014, **6**, 13440.
22 B. F. Cao, G. M. Veith, J. C. Neuefeind, R. R. Adzic and P. G. Khalifah, *J. Am. Chem. Soc.,* 2013, **135**, 19186.
23 W. F. Chen, C. H. Wang, K. Sasaki, N. Marinkovic, W. Xu, J. T. Muckerman, Y. Zhu and R. R. Adzic, *Energy Environ. Sci.,* 2013, **6**, 943.
24 H. Vrubel and X. L. Hu, *Angew. Chem. Int. Ed.,* 2012, **51**, 12703.
25 W. Cui, N. Y. Cheng, Q. Liu, C. J. Ge, A. M. Asiri and X. P. Sun, *ACS Catal.*, 2014, **4**, 2658.
26 T. Ferri, D. Gozzi and A. Latini, *Int. J. Hydrogen Energy,* 2007, **32**, 4692.
27 L. Liao, J. Zhu, X. Bian, L. Zhu, M. D. Scanlon, H. H. Girault and B. Liu, *Adv. Funct. Mater.,* 2013, **23**, 5326.
28 P. Y. Ge, M. D. Scanlon, P. Peljo, X. J. Bian, H. Vubrel, A. O'Neill, J. N. Coleman, M. Cantoni, X. L. Hu, K. Kontturi, B. H. Liu and H. H. Girault, *Chem. Commun.,* 2012, **48**, 6484.
29 X. Huang, Z. Y. Zeng, Z. X. Fan, J. Q. Liu and H. Zhang, *Adv. Mater.,* 2012, **24**, 5979.
30 C. B. Ma, X. Y. Qi, B. Chen, S. Y. Bao, Z. Y. Yin, X. J. Wu, Z. M. Luo, J. Wei, H. L. Zhang and H. Zhang, *Nanoscale,* 2014, **6**, 5624.
31 E. G. S. Firmiano, M. A. L. Cordeiro, A. C. R. Rabelo, C. J. Dalmaschio, A. N. Pinheiro, E. C. Pereira and E. R. Leite, *Chem. Commun.,* 2012, **48**, 7687.
32 L. P. Jia, X. Sun, Y. M. Jiang, S. J. Yu and C. M. Wang, *Adv. Funct. Mater.,* 2014, doi: 10.1002/adfm.201401814.
33 H. Tang, K. P. Dou, C. C. Kaun, Q. Kuang and S. H. Yang, *J. Mater. Chem. A,* 2014, **2**, 360.
34 S. Sarkar and S. Sampath, *Chem. Commun.,* 2014, **50**, 7359.
35 W. F. Chen, J. T. Mucherman and E. Fujita, *Chem. Commun.,* 2013, **49**, 8896.
36 W. F. Chen, S. Lyer, S. Lyer, K. Sasaki, C. H. Wang, Y. M. Zhu, J. T. Mucherman and E. Fujita, *Energy Environ. Sci.,* 2013, **6**, 1818.
37 A. T. Garcia-Esparza, D. Cha, Y. Ou, J. Kubota, K. Domen and K. Takanabe, *ChemSusChem,* 2013, **6**, 168.
38 Q. Liu, J. Q. Tian, W. Cui, P. Jiang, N. Y. Cheng, A. M. Asiri and X. P. Sun, *Angew. Chem. Int. Ed.,* 2014, **126**, 6828.
39 Z. Y. Ji, X. P. Shen, J. L. Yang, G. X. Zhu and K. M. Chen, *Appl. Catal. B,* 2014, **144**, 454.
40 D. J. Du, M. H. Cao, X. Y. He, Y. Y. Liu and C. W. Hu, *Langmuir,* 2009, **25**, 7057.
41 R. Pasricha, S. Gupta and A. K. Srivastava, *Small,* 2009, **5**, 2253.
42 Y. Z. Zhou, J. Yang, T. T. He, H. F. Shi, X. N. Cheng and Y. X. Lu, *Small,* 2013, **9**, 3445.
43 L. B. Ma, X. P. Shen, G. X. Zhu, Z. Y. Ji and H. Zhou, *Carbon,* 2014, **77**, 255.
44 C. J. Kim, W. Khan and S. Y. Park, *Chem. Phys. Lett.,* 2011, **511**, 110.
45 Z. Y. Ji, X. P. Shen, G. X. Zhu, H. Zhou and A. H. Yuan, *J. Mater. Chem.,* 2012, **22**, 3471.
46 X. H. Li, W. C. H. Choy, X. G. Ren, D. Zhang and H. F. Lu, *Adv. Funct. Mater.,* 2014, **24**, 3114.
47 D. Graf, F. Molitor, K. Ensslin, C. Stampfer, A. Jungen, C. Hierold and L. Wirtz, *Nano Lett.,* 2007, **7**, 238.
48 A. Barras, M.R. Das, R.R. Devarapalli, M.V. Shelke, S. Cordier, S. Szunerits and R. Boukherroub, *Appl. Catal. B,* 2013, **130**, 270.

49 J. Chang, M. H. Jin, F. Yao, T. H. Kim, V. T. Le, H. Y. Yue, F. Gunes, B. Li, A. Ghosh, S. S. Xie and Y. H. Lee, *Adv. Funct. Mater.,* 2013, **23**, 5074.
50 X. S. Qi, Y. Deng, W. Zhong, Y. Yang, C. Qin and C. Au, *J. Phys. Chem. C,* 2010, **114**, 808.
51 C. Wang, Z. Y. Guo, W. shen, Q. J. Xu, H. M. Liu and Y. G. Wang, *Adv. Funct. Mater.,* 2014, **24**, 5511.
52 K. T. Lee, J. C. Lytle, N. S. Ergang, S. M. Oh and A. Stein, *Adv. Funct. Mater.,* 2005, **15**, 547.
53 C. N. R. Rao, A. K. Sood, K. S. Subrahmanyam and A. Govindaraj, *Angew. Chem. Int. Ed.,* 2009, **48**, 7752.
54 M. S. Dresselhaus, A. Jorio, M. Hofmann, G. Dresselhaus and R. Saito, *Nano Lett.*, 2010, **10**, 751.
55 M. M. Lucchese, F. Satavle, E. H. Martins Ferreira, C. Vilani, M. V. O. Moutinho, R. B.Capaz, C. A. Achete and A. Jorio, *Carbon,* 2010, **48**, 1592.
56 Y. Y. Wen, H. M. Ding and Y. K. Shan, *Nanoscale,* 2011, **3**, 4411.
57 L. Liao, S. N. Wang, J. J. Xiao, X. J. Bian, Y. H. Zhang, M. D. Scanlon, X. L. Hu, Y. Tang, B. H. Liu, H. H. Girault, *Energy Environ. Sci.*, 2014, **7**, 387.
58 X. Sun, J. Dai, Y. Q. Guo, C. Z. Wu, F. T. Hu, J. Y. Zhao, X. C. Zeng and Y. Xie, *Nanoscale,* 2014, **6**, 8359.
59 H. Nolan, N. McEvoy, M. Obrien, N. C. Berner, C. Y. Yim, T. Hallam, A. R. McDonald and G. S. Duesberg, *Nanoscale*, 2014, **6**, 8185.
60 C. L. Choi, J. Feng, Y. G. Li, J. Wu, A. Zak, R. Tenne and H. J. Dai, *Nano Res.,* 2013, **6**, 921.
61 Y. Liang, Y. Li, H. Wang and H. Dai, *J. Am. Chem. Soc.,* 2013, **135**, 2013.
62 H. Huang and X. Wang, *J. Mater. Chem. A,* 2014, **2**, 6266.
63 K. P. de Jong, *Curr. Opin. Solid State Mater. Sci.,* 1999, **4**, 55.
64 J. O. M. Bockris and E. C. Potter, *J. Electrochem. Soc.,* 1952, **99**, 169.
65 Z. P. Huang, Z. B. Chen, Z. Z. Chen, C. C. Lv, H. Meng and C. Zhang, *ACS Nano,* 2014, **8**, 8121.
66 W. C. Sheng, H. A. Gasteiger and Y. Shao-Horn, *J. Electrochem. Soc.,* 2010, **157**, B1529.
67 X. Cao, Y. Han, C. Z. Gao, Y. Xu, X. M. Huang, M. Willander and N. Wang, *Nano Energy*, 2014, **9**, 301.
68 R. Ojani, R. Valiollahi and J. Raoof, *Energy*, 2014, **74**, 871.
69 R. Ojani, J. B. Raoof and E. Hasheminejad, *Int. J. Hydrogen Energy*, 2013, **38**, 92.
70 J. B. Raoof, R. Ojani, S. A. Esfeden and S. R. Nadimi, *Int. J. Hydrogen Energy*, 2010, **35**, 3937.
71 S. Bai, C. M. Wang, M. S. Deng, M. Gong, Y. Bai, J. Jiang and Y. J. Xiong, *Angew. Chem. Int. Ed.*, 2014, **53**, 12120.
72 A. Abbaspour and F. N. Sarvestani, *Int. J. Hydrogen Energy*, 2013, **38**, 1883.
73 D. S. Kong, J. J. Cha, H. T. Wang, H. R. Lee and Y. Cui, *Energy Environ. Sci.,* 2013, **6**, 3553.
74 Y. D. Ma, Y. Dai, M. Guo, C. W. Niu and B. B. Huang, *Nanoscale,* 2011, **3**, 3883.

